Experiments in Fluids (2023) 64:154
https://doi.org/10.1007/s00348-023-03697-6

RESEARCH ARTICLE

Single-camera PTV within interfacially sheared drops in microgravity

Patrick M. McMackin[1] · Joe A. Adam[2,3,4] · Frank P. Riley[5] · Amir H. Hirsa[2,4]

Received: 10 January 2023 / Revised: 8 August 2023 / Accepted: 18 August 2023 / Published online: 4 September 2023

Abstract

Development of experimental methods for in situ particle tracking velocimetry (PTV) is fundamental for allowing measurement of moving systems non-tailored for velocimetry. This investigation focuses on the development of a post-processing methodology for single-camera PTV, without laser-sheet illumination, tracking native air bubbles as tracer particles within a liquid drop of human insulin in microgravity. Human insulin functioned as a sufficiently complex, non-Newtonian fluid system for testing fluid measurement methodology. The PTV scenario was facilitated by microgravity technology known as the ring-sheared drop (RSD), aboard the International Space Station, which produced an optical imaging scenario and fluid flow geometry suitable as a testbed for PTV research. The post-processing methodology performed included five steps: (i) physical system characterization and native air bubble tracer identification, (ii) image projection and single-camera calibration, (iii) depth determination and 3D particle position determination, (iv) ray tracing and refraction correction, and (v) particle history and data expansion for suboptimal particles. Overall, this post-processing methodology successfully allowed for a total of 1085 particle measurements in a scenario where none were previously possible. Such post-processing methodologies have promise for application to other in situ PTV scenarios allowing better understanding of physical systems whose flow is difficult to measure and/or where PTV-specific optical elements (such as laser light sheets and dual-camera setups) are not permissible due to physical or safety constraints.

1 Introduction

Particle tracking velocimetry (PTV) algorithms are a class of numerical methods that determine the displacement of tracer particles in an image sequence to calculate velocity in time and space. Measurement of the velocity field is fundamental in understanding the behavior of flowing systems. In nature, flow measurements have the possibility to describe systems ranging from molecular biology (Faez et al. 2015; Huang and Choma 2015; Wang et al. 2018; Bos et al. 2021) and cellular biology (Marin et al. 2017; Wang et al. 2020; Savorana et al. 2022) to physiology (Sampath et al. 2018; Oeler et al. 2021; Zhang et al. 2022) and environmental (Gaudin et al. 2014; Aksamit and Pomeroy 2016; Mujtaba and de Lima 2018; Tauro et al. 2019; Tagliavini et al. 2022) science. Applied engineering systems whose performance analyses depend on fluid flow measurement span from biochemical reactors (Devasenathipathy et al. 2002; Kováts et al. 2018; Romano et al. 2021; Hofmann et al. 2022; Romano et al. 2023) and fundamental fluid dynamics (Humphrey et al. 1974; Kasagi and Nishino 1991; Kim et al. 2016) to manufacturing (Eschner et al. 2019; Fischer et al. 2022) and civil

✉ Amir H. Hirsa
hirsaa@rpi.edu

Patrick M. McMackin
mcmackinp2@gmail.com

Joe A. Adam
jadam3294@gmail.com

Frank P. Riley
frank97riley@gmail.com

[1] ADaPS, Boeing Defense, Space & Security, Huntsville, AL 35824, USA

[2] Mechanical, Aerospace and Nuclear Engineering, Rensselaer Polytechnic Institute, Troy, NY 12180-3590, USA

[3] Department of Biological Sciences, Rensselaer Polytechnic Institute, Troy, NY 12180-3590, USA

[4] Chemical and Biological Engineering, Rensselaer Polytechnic Institute, Troy, NY 12180-3590, USA

[5] Department of Propulsion and Power Engineering, NAVAIR, Patuxent River, MD 20670, USA

(Bautista-Capetillo et al. 2014; Fu et al. 2015; Zhao et al. 2020) industry. The imaging system must fulfill resolution requirements relative to the physical system; however, no constraint is imposed on the overall scale of the physical system, PTV being applicable to nano, (Faez et al. 2015; Matsuura et al. 2018; Wang et al. 2018; Bos et al. 2021; Satake 2022) micro, (Devasenathipathy et al. 2002; Fan et al. 2010; Choi et al. 2012; Huang and Choma 2015; Marin et al. 2017; Kawaguchi et al. 2019; Landauer et al. 2019; Dehnavi et al. 2020; McGlynn et al. 2020; Wang et al. 2020, 2020; Savorana et al. 2022) meso, (Humphrey et al. 1974; Kasagi and Nishino 1991; Boukany and Wang 2008; Gaudin et al. 2014; Kim et al. 2016; Lee et al. 2019) and macroscale (Bautista-Capetillo et al. 2014; Fu et al. 2015; Aksamit and Pomeroy 2016; Zhao et al. 2020) systems. Selection of tracer particles and advanced post-processing analyses can improve PTV algorithms allowing in situ velocimetry measurement in previously unsuitable, sensitive, or inaccuracy-prone systems.

Many PTV methods involve the addition of an easily-resolvable, minimally-invasive tracer particle to a physical system, often with further adjustment for PTV measurements including multi-camera or scanning optics, illumination such as laser sheets, and system isolation or refinement from a purely natural state (Uemura et al. 2012; Maas et al. 1993; Malik et al. 1993; Hoyer et al. 2005; Parker et al. 2022). In some physical systems, the impact of added tracers unacceptably alters system behavior. However, the possibility exists for using elements native to a system as tracer particles if these system elements can be resolved by the imaging system (Bautista-Capetillo et al. 2014; Gaudin et al. 2014; Faez et al. 2015; Aksamit and Pomeroy 2016; Ziegenhein et al. 2016; Wang et al. 2018, 2020; Bos et al. 2021; Choi et al. 2022; de Cerqueira et al. 2023). Another difficulty with many systems is that the optimization of PTV setups is often restricted, involving only a single point of view, complex geometry, or scenarios unsuitable for planar illumination or adding seeding particles as tracers. Efforts to extract accurate and minimally-invasive velocimetry data from a system form the field of PTV algorithm research. PTV algorithm research features investigations with single-camera views, (Hou et al. 2021; Noto et al. 2021; Fischer et al. 2022) novel experimental setups, (Sokoray-Varga and Józsa 2008; Choi et al. 2012; Bautista-Capetillo et al. 2014; Guo et al. 2014; Dal Sasso et al. 2018; Mujtaba and de Lima 2018; Landauer et al. 2019; Sabbagh et al. 2020; Parker et al. 2022; de Cerqueira et al. 2023) and analysis of numerical (Lei et al. 2012; Patel et al. 2018; Toeneboehn et al. 2018; Tauro et al. 2019; Janke et al. 2020; Mallery et al. 2020; Puzyrev et al. 2020; Zhao et al. 2020; Azadi et al. 2021; Cai et al. 2021; Qureshi et al. 2021; Sciacchitano and Discetti 2022) methods. All such investigations require simplified, yet sufficiently descriptive, experimental flow geometries as testbeds for the assessment of algorithm performance.

Flow within drops produces a 3D flow geometry that provides a useful and physically-rich scenario for developing novel velocimetry methods. Further, drop research is central to many developing technologies including biological assays, (Guo et al. 2012; Garcia-Cordero and Fan 2017; Kaminski and Garstecki 2017) droplet and contact line PTV, (Humphrey et al. 1974; Trantum et al. 2013; Bautista-Capetillo et al. 2014; Kvon et al. 2020; Fischer et al. 2022; de Cerqueira et al. 2023) material actuators, (Malouin Jr et al. 2011; Vogel and Steen 2010) adaptive optics, (López et al. 2005; López and Hirsa 2008; Dean and Hirsa 2015; Tyson and Frazier 2022) and manufacturing (Schuöcker et al. 2012; Murr and Johnson 2017; Scheithauer et al. 2017; Gilani et al. 2021; Lanzerotti et al. 2021) methods. The study of drop fluid dynamics is uniquely suited to experimentation in microgravity. In microgravity, air–liquid interfacial effects such as surface tension dominate, leading to drops with higher stability and larger achievable sizes compared to those on Earth. With this dominance of the interface in microgravity, many space-related problems in drop dynamics arise including fluid physics and contact line dynamics, (Trinh and Depew 1993; Pojman et al. 2007; Brutin et al. 2009; Derkach et al. 2009; Xu et al. 2011; Bába et al. 2019; Torres and Weislogel 2021; Amberg 2022; Ludwicki et al. 2022) combustion, (Dietrich et al. 2014; Guo et al. 2022; Meyer et al. 2022) technology adaptation for space, (Rizzardi et al. 2016; Reitz et al. 2021; Tamim and Bostwick 2021; McMackin et al. 2022b; Weislogel et al. 2022) and even rheology of planetary (Correia et al. 2014; Samuel et al. 2019; Suresh and Simranjeet 2020) bodies. Microgravity research is further translatable to science on Earth, as the overall benefit to humanity is a central focus of technologies for space exploration.

The ring-sheared drop (RSD) is a microgravity technology aboard the International Space Station (ISS) for complex fluid research, in situ experimental instrumentation, and biochemical reactor investigations. The RSD consists of a surface tension-contained drop, nominally 2.54 cm in diameter, pinned between two contact rings, one stationary and one rotating, which transmit shear via the drop's surface shear viscosity and produce mixing through secondary inertial flow (Fig. 1) (Gulati et al. 2017, 2018, 2019; Riley et al. 2021; McMackin et al. 2020, 2022a). The original investigation (2019 and 2021 ISS flight campaigns) of the RSD (McMackin et al. 2022a) focused on the effects of interfacial shear on the fibrillization kinetics (amyloidogenesis) of human insulin, centering on flow's effect on the biological system. Aqueous solutions of human insulin are interfacially active, producing complex non-Newtonian fluids with air–liquid interfaces exhibiting substantial changes in surface tension, and surface shear viscosity (McBride et al. 2015, 2016; Balaraj et al. 2017). Changes in

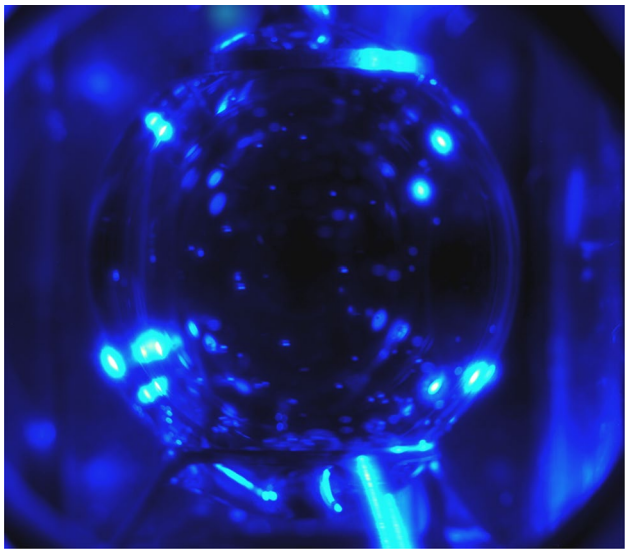

Fig. 1 Ring-sheared drop (RSD) containing a native 8 mg/mL human insulin solution showing air bubbles used as tracer particles. Here, the top contact ring is stationary, and the bottom rotates at 30 rpm

the biological system also produce reciprocal changes in fluid flow. The rich fluid behavior of insulin and other complex fluids of similar proteins require sophisticated surface modeling that, in turn, depends on validation using accurate experimental measurements. Here, insulin solutions act as a model complex fluid for testing the efficacy of novel PTV methodologies for validating complex fluid simulations. In this investigation, alterations in fluid behavior were originally designed to be studied using velocimetry within a narrow field of view limited to only the fluid interface, without bulk data. Further PTV limitations were imposed by ISS safety constraints regarding the use of large laser light sheets. However, protein solution freezing, thawing, handing, and deployment produced air bubbles usable as tracer particles. This serendipitous occurrence of air bubbles allowed for PTV to be performed at the full scale of the drop throughout much of the drop's volume. This investigation focuses on the development of a PTV processing method for in situ determination of velocimetry, hypothesizing that if a suboptimal in situ PTV scenario is supported by suitable post-processing methodology, then useful 3D velocimetry data can be acquired within a non-PTV-tailored system.

2 Methods

2.1 Physical system

The physical system consisted of a solution of human insulin (Sigma-Aldrich 91077C). This investigation focused on a single concentration of native (unfibrillized) 8 mg/mL insulin in an aqueous buffer (0.1 M NaCl 1.6 pH) which was pH cycled with HCl and NaOH (Posada et al. 2012; Adam et al. 2021; McMackin et al. 2022a). After preparation, samples were degassed at 710 mmHg for 0.5 days, frozen at − 20 °C, transported to the ISS, and maintained for several months at − 80 °C then eventually allowed to thaw at room temperature for 1 day prior to experimentation. Sample preparation followed the same methodology as in ground control experiments (Adam et al. 2021). The solution examined by PTV in this investigation is one of the cases performed in the 2021 ISS flight campaign along with the steady shear-fibrillization protein kinetics (McMackin et al. 2022a) trials.

Human insulin, like many proteins and biopolymers, is surface active, (Edwards et al. 1991; Adamson and Gast 1997; Doi 2013) having more stable energetic states at the interface. The alteration of fluid properties due to molecular adsorption produces complex fluids with non-Newtonian interfaces, whose motion can be modeled using interfacial boundary conditions such as the Boussinesq–Scriven surface model (further detailed in the Results section). The increased intricacy of such mathematical models requires experimental validation with methods capable of measuring the differences in fluid motion caused by the presence of proteins. The PTV post-processing algorithm in this investigation was tested using human insulin solutions for the purpose of developing a sufficiently accurate methodology for application to complex fluids. In addition to the alteration of fluid properties, the clustering of insulin at an interface can also produce a stabilizing effect, in part responsible for the visual 'soapiness' of insulin solutions and the stability of the serendipitous air bubbles, with bubbles rarely coalescing or rupturing (dissolution into solution occurring on time scales on the order of days). This constant size and stability of air bubbles over the 4-s PTV video capture period ensured their suitability as essentially invariant tracer particles. The flow parameterization furthermore suited PTV analysis, with two full revolutions of the shearing bottom ring occurring over 4 s at 30 rpm. Fluid flow produced at these conditions had characteristic Reynolds number of 180 ($\mathrm{Re} = \Omega^* a^2/\nu$) and Boussinesq number of ~ 6 (Balaraj et al. 2017) ($\mathrm{Bo} = \mu^s/(\mu^* a)$) (Edwards et al. 1991). Here, Ω is the rotating ring's angular velocity, a is the characteristic length scale equal to the ring radius 0.76 cm, ν is kinematic viscosity

$0.0096\ \mathrm{cm}^2/s$, μ is dynamic shear viscosity 0.0094 g/(cm*s), and μ^s is surface shear viscosity 0.043 g/s; all viscosities measured for the native 8 mg/mL insulin solution using a Cannon–Fenske viscometer (μ) and deep-channel surface viscometer (μ^s).

2.2 Image projection

The first step of particle tracking is to project the pixel values, x_{px}, of a feature location onto the x–z plane in Cartesian coordinates, x. For an ideal camera, this change of coordinates can be performed using an affine transformation given as $x = \mathbf{K}^{-1}x_{px} - b$. This transformation can be expanded as follows:

$$\begin{bmatrix} x \\ y \\ z \end{bmatrix} = \begin{bmatrix} d_x & n/2 & -\alpha \\ 0 & m/2 & -d_y \\ 0 & 1 & 0 \end{bmatrix}^{-1} \begin{bmatrix} x_{px} \\ y_{px} \\ 1 \end{bmatrix} - \begin{bmatrix} 0 \\ 1 \\ 0 \end{bmatrix}, \tag{1}$$

$$\text{and} \quad d_x = \frac{n/2}{\tan(H_{fov}/2)}, \quad d_y = \frac{m/2}{\tan(V_{fov}/2)}. \tag{2}$$

Variables in this transformation are, m the image row number, n the image column number, H_{fov} the horizontal field of view angle, V_{fov} the vertical field of view angle, and α the camera sensor's skewness. Square pixels, $d_x = d_y$, and no skew, $\alpha = 0$, can be assumed for this camera configuration, shown in Fig. 2. This transformation converts the locations of objects detected on the camera's sensor from pixel values of the form $[x_{px}, y_{px}, 1]^T$, to focal length-normalized Cartesian coordinates with the from $[x, y, z]^T$. For improved analysis efficiency in this drop geometry, $\mathbf{K}$ uses a slightly different form from other common camera calibration matrices, (Christian and Crassidis 2021) centering the coordinate frame within the sphere (see Fig. 2) such that the z–axis is the axis of the drop's rotation.

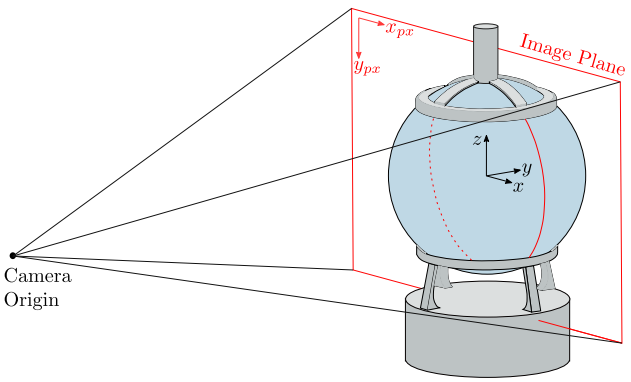

Fig. 2 Schematic of the camera's projected image plane in relation to the system's x-y plane. The camera calibration matrix, $\mathbf{K}$, converts feature locations in pixel values (x_{px}, y_{px}) to physical Cartesian coordinates (x, y, and z), accounting for the drop's geometry

2.3 Depth determination

Projecting sensor data onto the image plane does not fully resolve true particle location. The single-camera PTV used for the RSD restricted data collection to one full-field camera view, with particle depth determined by position tracking in time throughout drop rotation. Further, this depth determination required the assumption of axisymmetric flow, particles moving in circular constant radius paths. A particle moving at a constant angular velocity, when viewed in the camera-observed x–z plane, appears to translate in the x-direction at a non-constant velocity. During a full drop rotation, a particle will reach an apex in the x-direction, intercepting the x–z plane (Fig. 3). At this maximum distance in the x-direction (or identically when $\partial x/\partial t = \partial x_{px}/\partial t = 0$), the exact position of the particle in 3D space is known. Subsequently, assuming constant radial position (that the radial velocity component is much smaller than the primary azimuthal velocity component, $\partial r/\partial t \to 0$, (Gulati et al. 2018, 2019)) allows single-camera determination of 3D particle position in all frames.

Depth determination requires calculation of where an individual ray intersects the surface of a sphere of radius r (r defined above as the maximum axisymmetric x-direction path distance). The intersecting ray in question is the vector connecting the camera's origin to the apparent location of the particle in the image plane (black arrow in Fig. 3b). The parametric representation of all points on this line in space can be given as follows:

$$P_{\mathrm{L}}(t_p) = P_0 + \hat{P}t_p. \tag{3}$$

Here P_0 is the origin of the line, the camera sensor, $\hat{P}$ is the unit vector describing the line's direction, and t_p is a parameter used to describe an individual point on the line, P_{L}. In this application, $t_p > 0$ for all data points (forward facing vectors only). The intersection of this projected line with a

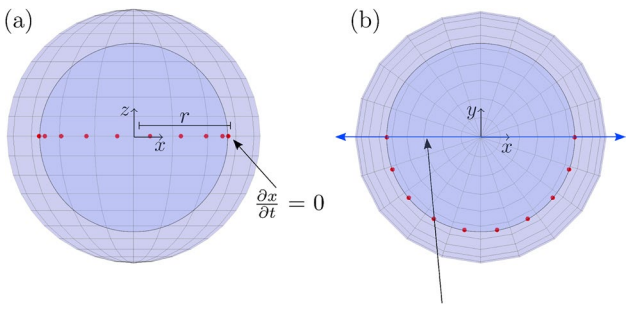

Fig. 3 Schematic example of a particle at constant radial position and constant angular velocity moving within a sphere viewed from the **a** camera and **b** top–down point of view

sphere of radius r can be solved for analytically. The collection of all points, P_S, on the surface of a sphere with radius r centered at $c = (x_0, y_0, z_0)$ is given as follows:

$$(x - x_0)^2 + (y - y_0)^2 + (z - z_0)^2 = \|P_S - c\|^2 = (P_S - c) \cdot (P_S - c) = r^2. \tag{4}$$

Substituting $P_L = P_S$ in Eq. 4 allows rearrangement of the function (Shirley 2020) and solution of the intersection between a line and the surface of a sphere in the form of a quadratic function in terms of the parameter t_p:

$$\left[\hat{P} \cdot \hat{P}\right] t_p^2 + \left[\hat{P} \cdot (P_0 - c)\right] t_p + \left[(P_0 - c) \cdot (P_0 - c)\right] = 0. \tag{5}$$

The value of the parameter that denotes the intersection of the line and sphere, t_{pI}, can be solved via the quadratic equation:

$$t_{pI} = \frac{-\left[\hat{P} \cdot (P_0 - c)\right] \pm \sqrt{\left[\hat{P} \cdot (P_0 - c)\right]^2 - 4\left[\hat{P} \cdot \hat{P}\right]\left[(P_0 - c) \cdot (P_0 - c)\right]}}{2\left[\hat{P} \cdot \hat{P}\right]}. \tag{6}$$

The sign of the discriminant determines the type of intersection: Negative values result for lines which do not intersect the sphere, zero indicates lines tangent to the sphere intersecting at only one point, and positive values result from lines with two points of intersection. In this application, only discriminants ≥ 0 are possible as air bubbles are assumed to remain in a circular path within the drop. Furthermore, like t_p, t_{pI} must be > 0 for valid, forward-facing solutions. With these assumptions, the point of intersection, P_I, can now be directly calculated:

$$P_I = P_L(t_{pI}). \tag{7}$$

For the realistic case of two intersection points, the point closer to the camera origin is the correct solution, as particles in the back half of the drop are not resolvable from image data. Using this near-intersect assumption, an estimate of 3D particle position including depth information can be calculated.

2.4 Ray tracing

Light scattered from air bubble tracer particles within the RSD passed through the drop's liquid bulk and the test cell's air interior before reaching the camera's sensor. The differences in refractive index between these materials was accounted for when estimating a particle's position in 3D space (paths depicted in Fig. 4). This correction was performed using a ray-tracing analysis, modeling the path of light from the camera's sensor to the particle (Heckbert and Hanrahan 1984).

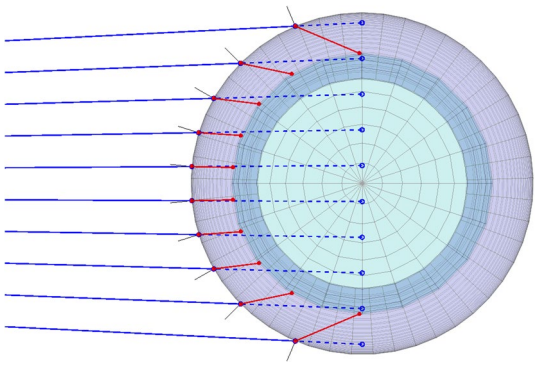

Fig. 4 Top–down schematic of the ray-tracing technique correcting 3D particle position for refractive index mismatch and drop non-sphericity. Lines represent: (blue) camera sensor particle position $\hat{P}$, (red) refraction corrected transmitted path $\hat{T}$, and (black) non-sphericity corrected surface normal unit vectors $\hat{N}$

A ray of light's path after intersecting the sphere's interface can be determined using Snell's law, which relates the the angle of transmission, θ_t, and the angle of incidence, θ_i, to the refractive index ratio of two media, η:

$$\frac{\sin(\theta_t)}{\sin(\theta_i)} = \frac{\eta_i}{\eta_t} = \eta. \tag{8}$$

The transmission unit vector, $\hat{T}$ (angled by θ_t), can be represented in terms of $\hat{N}$ and $\hat{M}$, the unit vectors for the planes normal and tangent planes to the intersected surface:

$$\hat{T} = \sin(\theta_t)\hat{M} - \cos(\theta_t)\hat{N} \tag{9}$$

Snell's law can be utilized to calculate $\hat{T}$ as a function of the incident unit vector ($\hat{I}$), surface normal ($\hat{N}$), and index of refraction ratio (η) as shown in Eqns. 10–14: (Foley et al. 1996)

$$\hat{M} = \frac{\hat{N}\cos(\theta_i) - \hat{I}}{\sin(\theta_i)}, \tag{10}$$

$$\hat{T} = (\eta\cos(\theta_i) - \cos(\theta_t))\hat{N} - \eta\hat{I}, \tag{11}$$

$$\cos(\theta_i) = \hat{N} \cdot \hat{I}, \tag{12}$$

$$\cos(\theta_t) = \sqrt{1 - \sin^2(\theta_t)} = \sqrt{1 - \eta^2\sin^2(\theta_i)} = \sqrt{1 - \eta^2(1 - (\hat{N} \cdot \hat{I})^2)}, \tag{13}$$

$$\hat{T} = \left(\eta(\hat{N} \cdot \hat{I}) - \sqrt{1 - \eta^2(1 - (\hat{N} \cdot \hat{I})^2)}\right)\hat{N} - \eta\hat{I}. \tag{14}$$

Values of η, $\hat{I}$, and $\hat{N}$ are required to calculate $\hat{T}$ using Eq. 14. η was assumed to be a constant, the ratio of air and water refractive indices, approximating the protein solution's

refractive index as that of water. For the determination of $\hat{N}$ and $\hat{I}$, the slight non-sphericity of the RSD's interface was quantified using the drop profile captured by the camera. Non-sphericity was a result of slight variations in deployment tube position, wetting, and total injected volume. Assuming axisymmetry, the 3D drop surface was defined by revolving the 2D surface profile of the interface in the plane of the camera, $x = f(z)$, about the vertical axis. Substituting $r^2 = f(z)^2 + z^2$ and assuming the drop's center to be at the origin (Eq. 4), the revolved surface produced, S, is: (Gray 1996)

$$S(x, y, z) = f(z) - \sqrt{x^2 + y^2} = 0. \tag{15}$$

Determining the intersection of the drop's surface and a ray of light from the camera's sensor can be performed using the line parameterization in Eq. 3:

$$F(t) = S\left(x_0 + t_p\hat{p}_x, y_0 + t_p\hat{p}_y, z_0 + t_p\hat{p}_z\right) = 0, \tag{16}$$

where

$$P_0 = (x_0, y_0, z_0) \quad \text{and} \quad \hat{P} = \left(\hat{p}_x, \hat{p}_y, \hat{p}_z\right). \tag{17}$$

$F(t) = 0$, solved iteratively for the parameter t_{pI}, determines the intersection point of the incident line $\hat{I}$ and the surface S. Here, the Newton–Raphson method was utilized with an initial guess of t_{pI} equal to the analytical solution of a line–sphere intersection (as presented in Sect. 2.3). The solution for $\hat{I}$ can then be used to determine the surface normal, $\hat{N}$. Parameterizing the same revolved surface in cylindrical coordinates (azimuthal angle of revolution, ϕ, and the vertical axis, z): (do Carmo 1976)

$$S(\phi, z) = \left[f(z)\cos(\phi), f(z)\sin(\phi), z\right]. \tag{18}$$

The unit normal can be taken as follows:

$$\hat{N} = \frac{S_\phi \times S_z}{\|S_\phi \times S_z\|}, \tag{19}$$

where the partial derivatives are given as follows:

$$S_\phi = \frac{\partial S}{\partial \phi} = \left[-f(z)\sin(\phi), f(z)\cos(\phi), 0\right], \tag{20}$$

and

$$S_z = \frac{\partial S}{\partial z} = \left[\frac{\partial f(z)}{\partial z}\cos(\phi), \frac{\partial f(z)}{\partial z}\sin(\phi), 1\right]. \tag{21}$$

After solving for $\hat{N}$, Eq. 14 can be used to determine the direction of the transmitted ray into the drop's bulk. The refraction-corrected location of a particle can then be determined by the intersection of $\hat{T}$ with an origin-centered sphere of radius equal to the radial distance determined for a particle via the tracking method described in Sect. 2.3. This correction technique for particle location in a non-index-matched, non-spherical drop is depicted in Fig. 4.

2.5 Particle history

Extrapolation of particle path history can be used to measure the velocity of particles which do not intersect the camera's projected image plane during the time frame of data acquisition. A particle may not intersect the camera's projected image plane for a multitude of reasons including loss of sight (fluid turbidity, particle size, and optics) and particle motion dynamics (initial position and speed). These non-image-plane-intersecting particles cannot be assigned a path radius, preventing their use as viable tracer particles. However, if a non-image-plane-intersecting particle can be tracked for a sufficient number of frames, the resulting horizontal component of velocity can be fit to a characteristic particle motion function such that the location of the x–z plane intersection ($\partial x/\partial t = \partial x_{px}/\partial t = 0$) can be extrapolated. This characteristic particle motion function must be tailored to the flow characteristics and assumptions in the observed system.

Using the assumption of axisymmetry, a constant path radius particle at constant azimuthal velocity would appear to translate from left to right in the camera's projected image plane with a sinusoidal motion, resulting in harmonic $\partial x_{px}/\partial t$. However, the effect of refractive index mismatch produces non-harmonic characteristic particle motions in the camera sensor. Empirical models for the characteristic apparent horizontal velocity of a particle in camera sensor pixel coordinates, $g(x_{px}) = \partial x_{px}/\partial t$, were developed by tracking the motion of fully-resolvable test particles. A number of characteristic functions with different forms were analyzed, the results of which are presented in Table 1, which assesses the performance of a fit by the root-mean-square (RMS) error as a percentage of the characteristic length scale, ring radius, a. A secant function was found to best fit velocimetry data at the most relevant particle depths. Applying this particle history extrapolation technique, the path radius of well-tracked non-image-plane-intersecting particles can be determined, resulting in increased flow field data resolution totaling 1085 data points.

Table 1 The root-mean-square (RMS) error as a percentage of the characteristic length scale ring radius, a, for each empirical characteristic apparent horizontal velocity model

Function	Form	RMS error (%)
Cosine	$g(x_{px}) = p_1 \cos(p_2 x_{px})$	0.117
Parabola	$g(x_{px}) = p_1 x_{px}^2 + p_2 x_{px} + p_3$	0.088
Ellipse	$g(x_{px}) = \sqrt{(1 - x_{px}^2/p_1^2)p_2^2}$	0.040
Secant	$g(x_{px}) = p_1 \sec((x_{px}/p_2) + p_3)$	0.020

3 Results

The post-processing methodology in support of the in situ multi-phase air bubble PTV within the RSD in the Fall 2021 ISS campaign analyzing a native 8 mg/mL human insulin solution was found to reliably resolve bulk velocity measurements between $0.4 \lesssim r/R \lesssim 0.8$, $\|\theta\| \lesssim 60°$, and $\|\phi\| \lesssim 60°$ (r, θ, and ϕ are radial, polar, and azimuthal spherical coordinates, and $[\phi, \theta] = 0°$ is defined by the vector connecting the camera to the RSD's center). Measurements assumed axisymmetry tracer motion for depth determination and particle history calculations. The range of r was limited by the positions of air bubble tracers. The polar angle θ was limited by occlusion from the top and bottom rings. Azimuth angle ϕ was limited by the inability to resolve particles in the back half of the drop and noise increasing proportionally with $1/\cos\phi$ from the geometry involved in this technique. The volume of individual gas bubbles was not found to have any correlation with velocity data produced, further validating their utility as tracer particles.

The validity of this post-processing methodology was assessed by comparing normalized azimuthal velocity ($v_\phi/(\Omega * a)$) acquired by PTV measurements to velocity calculated by a numerical simulation of the flow within the RSD (Fig. 5). The use of human insulin solutions, whose fluid parameters are non-Newtonian, allowed determination of PTV algorithm performance when measuring a complex fluid system in comparison with a mathematical model. The simulation used a Boussinesq–Scriven surface model with a Newtonian bulk (modified from a previous theoretical model (Gulati et al. 2019)) with flow properties matched to experimental parameters and material properties of a native 8 mg/mL human insulin solution (Re = 180 and Bo = 6). Exact modifications to the COMSOL model included no-slip boundaries better approximating a rotating ring and stationary cap, as well as updated material properties for human insulin at 8 mg/mL. The 266,952 domain element mesh consisted of finely distributed nodes at the interface with a boundary layer mesh of quadrilateral elements and a bulk of tetrahedral elements, overall with a maximum edge length of 0.25 mm or 0.03*a.

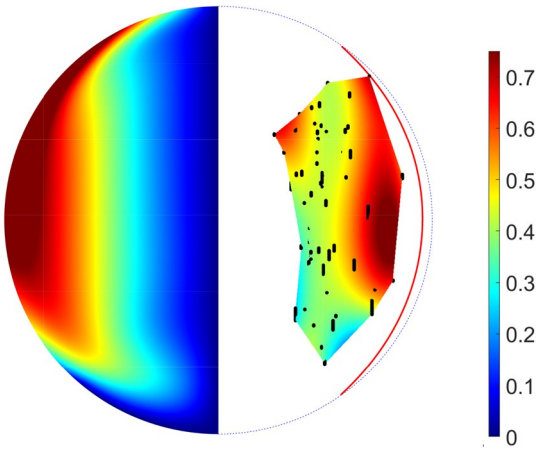

Fig. 5 RSD r-z plane color map of normalized azimuthal velocity ($v_\phi/(\Omega * a)$) for an 8 mg/mL native insulin solution shearing at 30 rpm (Re = 180 and Bo = 6). The left hemisphere presents computational results of a Boussinesq–Scriven surface model with a Newtonian bulk. The right hemisphere presents experimental measurements (1085 data points) obtained using the post-processing PTV methodology with air bubble tracer particles, the red line denoting the detected interface's departure from spherical

4 Discussion

This investigation focuses on the development of a post-processing methodology for improving PTV accuracy and precision of in situ non-PTV-tailored systems. The sequence of post-processing methods presented in this investigation can be extended to a more generalized analysis framework, applicable to systems outside this investigation's purview including different flow geometries, complex fluids with different behaviors, and unstable flow. The steps of this post-processing framework include: tracer identification (Methods Sect. 2.1, Physical System), camera calibration (Methods Sect. 2.2, Image Projection), location refinement (Methods Sect. 2.3, Depth Determination), optical refinement (Methods Sect. 2.4, Ray Tracing), and data expansion (Methods Sect. 2.5, Particle History). Such a framework is applicable to other in situ PTV scenarios, following these five steps each customized to the specific PTV application under consideration.

Validation of the experimental post-processing methodology for in situ PTV measurement was performed through comparison to a Boussinesq–Scriven surface model with a Newtonian bulk. The use of human insulin solutions with complex fluid behavior for PTV post-processing algorithm testing enabled algorithm validation not only for standard Newtonian fluids, but also demonstrated the algorithm's applicability to complex fluids. This comparison, presented in Fig. 5, displays a reasonable agreement between PTV experimental measurements and theoretical computations. The qualitative flow profile is well-matched within the accurate measurement area ($0.4 \lesssim r/R \lesssim 0.8$, $\|\theta\| \lesssim 60°$, and $\|\phi\| \lesssim 60°$), with dissimilarities occurring more frequently toward the edges of this region. Imprecision in the experimental PTV methodology arose from several sources: sparse non-uniform distribution of air bubble tracer particles, optical occlusion, and secondary flow effects. While serendipitous air bubbles served as the only tracer, their spatial distribution, size, and stability were uncontrolled, leading to variations which, respectively, reduced the available field of

measurable data, required variable particle size identification, and the possibility of particle loss by dissolution. Based on the orientation of the single camera, optical occlusion occurred by geometric structures (RSD rings) and signal reduction at further distances within the drop (far drop half). Post-processing assumed particles followed a constant radius circular path, incurring error due to the fact that secondary flow exists in the *r*-θ plane. Overall, this investigation's post-processing methodology for in situ PTV was successful in extracting full-field bulk velocimetry data, describing fluid motion in a scenario where such capture was not previously possible.

Further experimentation with PTV methods that could be assessed within the RSD include the study of tracer particle characteristics, fluid rheology, sub-system measurement, utilization of color data, and measurements of different flows experienced during drop deployment and extraction. The use of improved precision tracer particles, such as adding hollow glass microspheres, is currently under way to improve bulk velocimetry data in comparison with air bubble measurements (Fig. 5), allowing the quantification of method precision in relation to theory. Adjusting depth determination and particle history characteristic particle motion functions (such as those in Table 1) can be used to produce measurements of more complex flows, including those with instabilities and turbulence, with the potential to produce empirical flow models or validate novel theories of unstable flow. Rheological models of fluid behavior can be validated using PTV methods, comparing measurements to non-Newtonian or viscoelastic soft matter models. PTV measurement of sub-system regions within a larger system is also possible, potentially focusing on important phenomena such as wetting and contact line dynamics or effects of the fluid interface. RGB color data from the camera sensor, not utilized in this investigation, could be applied to dyes, fluorophores, and colored particles for multiple tracers in situ in situ PTV. Drop deployment and drop extraction present transient flow geometries that could test the performance of this PTV methodology on time-dependent flows. Each of these applications has the potential to improve applied PTV research and development, as well as benefit physical understanding of the systems being measured.

Acknowledgements The authors would like to thank Louise Littles, Sridhar Gorti, Hong Q. Yang, Kevin Depew, Michael Hall, James McClellan, Heidi Parris, Shawn Reagan, Ryan Reeves, Shawn Stephens, Paul Galloway, Ben Murphy, and Fran Chiramonte for their continued support of both the RSD project and the operations team at Rensselaer Polytechnic Institute. The authors also thank astronauts Raja Chari, Shane Kimbrough, Christina Koch, Akihiko Hoshide, Megan McArthur, Luca Parmitano, Thomas Pasquet, and Mark Vande Hei for their excellence and flexibility during real-time space operations. The authors are also grateful for the support to this study given by NASA BPS, NASA MSFC, NASA JSC, NSF-CASIS, and Teledyne-Brown Engineering.

Author contributions PM, JA, and AH conceptualized and designed the experiment. JA prepared insulin solutions. PM and JA performed the remote ISS operations and experimental measurements. PM performed the analysis of experimental measurements and developed the ray-tracing technique. FR performed supporting computational fluid dynamics simulations. PM and JA wrote the manuscript with support from AH and FR. All listed authors critically evaluated data and results, including data interpretation, figure development, and manuscript editing.

Funding This work was supported by NASA Grant 80NSSC20K1726 and NSF Grant 1929134.

Data/code availability The data and code corresponding to this study are available from the corresponding authors upon reasonable request.

Declarations

Conflict of interest The authors declare that they have no known conflict of interest or personal relationships that could have appeared to influence the work reported in this paper.

Ethics approval and consent to participate Not applicable.

Consent for publication The authors confirm that this work is original and has not been published elsewhere, nor is it under consideration for publication elsewhere, and consent for the publication in experiments in fluids.

References

Adam JA, Middlestead HR, Debono NE, Hirsa AH (2021) Effects of shear rate and protein concentration on amyloidogenesis via interfacial shear. J Phys Chem B 125(36):10355–10363. https://doi.org/10.1021/acs.jpcb.1c05171

Adamson AW, Gast AP (1997) Physical chemistry of surfaces, 6th edn. Wiley, New York

Aksamit NO, Pomeroy JW (2016) Near-surface snow particle dynamics from particle tracking velocimetry and turbulence measurements during alpine blowing snow storms. Cryosphere 10(6):3043–3062. https://doi.org/10.5194/tc-10-3043-2016

Amberg G (2022) Detailed modelling of contact line motion in oscillatory wetting. npj Microgravity 8(1):1. https://doi.org/10.1038/s41526-021-00186-0

Azadi R, Wong J, Nobes DS (2021) Determination of fluid flow adjacent to a gas/liquid interface using particle tracking velocimetry (PTV) and a high-quality tessellation approach. Exp Fluids 62(3):48. https://doi.org/10.1007/s00348-020-03103-5

Bába P, Tóth Á, Horváth D (2019) Surface-tension-driven dynamic contact line in microgravity. Langmuir 35(2):406–412. https://doi.org/10.1021/acs.langmuir.8b03592

Balaraj VS, Zeng PCH, Sanford SP, McBride SA, Raghunandan A, Lopez JM, Hirsa AH (2017) Surface shear viscosity as a macroscopic probe of amyloid fibril formation at a fluid interface. Soft Matter 13:1780–1787

Bautista-Capetillo C, Robles O, Salinas H, Playán E (2014) A particle tracking velocimetry technique for drop characterization in agricultural sprinklers. Irrig Sci 32(6):437–447. https://doi.org/10.1007/s00271-014-0440-6

Bos J, Cisneros LH, Mazel D (2021) Real-time tracking of bacterial membrane vesicles reveals enhanced membrane traffic upon antibiotic exposure. Sci. Adv. 7(4):eabd1033. https://doi.org/10.1126/sciadv.abd1033

Boukany PE, Wang SQ (2008) Use of particle-tracking velocimetry and flow birefringence to study nonlinear flow behavior of entangled wormlike micellar solution: from wall slip, bulk disentanglement to chain scission. Macromolecules 41(4):1455–1464. https://doi.org/10.1021/ma702527s

Brutin D, Zhu Z, Rahli O, Xie J, Liu Q, Tadrist L (2009) Sessile drop in microgravity: creation, contact angle and interface. Microgravity Sci Technol 21(S1):67–76. https://doi.org/10.1007/s12217-009-9132-x

Cai S, Li H, Zheng F, Kong F, Dao M, Karniadakis GE, Suresh S (2021) Artificial intelligence velocimetry and microaneurysm-on-a-chip for three-dimensional analysis of blood flow in physiology and disease. Proc Natl Acad Sci USA 118(13):e2100697118. https://doi.org/10.1073/pnas.2100697118

Choi YS, Seo KW, Sohn MH, Lee SJ (2012) Advances in digital holographic micro-PTV for analyzing microscale flows. Opt Lasers Eng 50(1):39–45. https://doi.org/10.1016/j.optlaseng.2011.06.023

Choi D, Kim H, Park H (2022) Bubble velocimetry using the conventional and CNN-based optical flow algorithms. Sci Rep 12(1):11879. https://doi.org/10.1038/s41598-022-16145-y

Christian JA, Crassidis JL (2021) Star identification and attitude determination with projective cameras. IEEE Access 9:25768–25794. https://doi.org/10.1109/ACCESS.2021.3054836

Correia ACM, Boué G, Laskar J, Rodríguez A (2014) Deformation and tidal evolution of close-in planets and satellites using a Maxwell viscoelastic rheology. Astron Astrophys 571:A50. https://doi.org/10.1051/0004-6361/201424211

Dal Sasso SF, Pizarro A, Samela C, Mita L, Manfreda S (2018) Exploring the optimal experimental setup for surface flow velocity measurements using PTV. Environ Monit Assess 190(8):460. https://doi.org/10.1007/s10661-018-6848-3

de Cerqueira RF, Perissinotto RM, Verde WM, Biazussi JL, de Castro MS, Bannwart AC (2023) Development and assessment of a particle tracking velocimetry (PTV) measurement technique for the experimental investigation of oil drops behaviour in dispersed oil–water two-phase flow within a centrifugal pump impeller. Int J Multiph Flow 159:104302. https://doi.org/10.1016/j.ijmultiphaseflow.2022.104302

Dean JL, Hirsa AH (2015) Performance of a microscope with an embedded oscillating pinned-contact liquid lens. Appl Opt 54(27):8228. https://doi.org/10.1364/AO.54.008228

Dehnavi PG, Wei D, Aubin-Tam ME, Tam DSW (2020) Optical tweezers-based velocimetry: a method to measure microscale unsteady flows. Exp Fluids 61(9):202. https://doi.org/10.1007/s00348-020-03031-4

Derkach SR, Krägel J, Miller R (2009) Methods of measuring rheological properties of interfacial layers (Experimental methods of 2D rheology). Colloid J 71(1):1–17. https://doi.org/10.1134/S1061933X09010013

Devasenathipathy S, Santiago JG, Takehara K (2002) Particle tracking techniques for electrokinetic microchannel flows. Anal Chem 74(15):3704–3713. https://doi.org/10.1021/ac011243s

Dietrich DL, Nayagam V, Hicks MC, Ferkul PV, Dryer FL, Farouk T, Shaw BD, Suh HK, Choi MY, Liu YC, Avedisian CT, Williams FA (2014) Droplet combustion experiments aboard the international space station. Microgravity Sci Technol 26(2):65–76. https://doi.org/10.1007/s12217-014-9372-2

do Carmo MP (1976) Differential geometry of curves and surfaces. Prentice Hall

Doi M (2013) Soft matter physics, 1st edn. Oxford University Press, Oxford, New York

Edwards DA, Brenner H, Wasan DT (1991) Interfacial transport processes and rheology. Butterworth-Heinemann series in chemical engineering. Butterworth-Heinemann, Boston

Eschner E, Staudt T, Schmidt M (2019) 3D particle tracking velocimetry for the determination of temporally resolved particle trajectories within laser powder bed fusion of metals. Int J Extrem Manuf 1(3):035002. https://doi.org/10.1088/2631-7990/ab3de9

Faez S, Lahini Y, Weidlich S, Garmann RF, Wondraczek K, Zeisberger M, Schmidt MA, Orrit M, Manoharan VN (2015) Fast, label-free tracking of single viruses and weakly scattering nanoparticles in a nanofluidic optical fiber. ACS Nano 9(12):12349–12357. https://doi.org/10.1021/acsnano.5b05646

Fan YJ, Sheen HJ, Liu YH, Tsai JF, Wu TH, Wu KC, Lin S (2010) Detection of C-reactive protein in evanescent wave field using microparticle-tracking velocimetry. Langmuir 26(17):13751–13754. https://doi.org/10.1021/la102137j

Fischer RD, Moaven M, Kelly D, Morris S, Thurow B, Prorok BC (2022) 3D tracking velocimetry of L-PBF spatter particles using a single high-speed plenoptic camera. Addit Manuf Lett 3:100083. https://doi.org/10.1016/j.addlet.2022.100083

Foley JD, van Dam A, Feiner SK, Hughes JF (1996) Computer graphics: principles and practice, in C, 2ed edn. Addison Wesley

Fu S, Biwole PH, Mathis C (2015) Particle Tracking Velocimetry for indoor airflow field: a review. Build Environ 87:34–44. https://doi.org/10.1016/j.buildenv.2015.01.014

Garcia-Cordero JL, Fan ZH (2017) Sessile droplets for chemical and biological assays. Lab Chip 17(13):2150–2166. https://doi.org/10.1039/C7LC00366H

Gaudin D, Moroni M, Taddeucci J, Scarlato P, Shindler L (2014) Pyroclast tracking velocimetry: a particle tracking velocimetry-based tool for the study of Strombolian explosive eruptions: pyroclast tracking velocimetry methods. J Geophys Res Solid Earth 119(7):5369–5383. https://doi.org/10.1002/2014JB011095

Gilani N, Aboulkhair N, Simonelli M, East M, Ashcroft I, Hague R (2021) Insights into drop-on-demand metal additive manufacturing through an integrated experimental and computational study. Addit Manuf 48:102402. https://doi.org/10.1016/j.addma.2021.102402

Gray A (1996) Modern differential geometry of curves and surfaces with Mathematica, 1st edn. CRC Press Inc., USA

Gulati S, Raghunandan A, Rasheed F, McBride SA, Hirsa AH (2017) Ring-sheared drop (RSD): microgravity module for containerless flow studies. Microgravity Sci Technol 29(1–2):81–89. https://doi.org/10.1007/s12217-016-9527-4

Gulati S, Riley FP, Lopez JM, Hirsa AH (2018) Mixing within drops via surface shear viscosity. Int J Heat Mass Transf 125:559–568. https://doi.org/10.1016/j.ijheatmasstransfer.2018.04.057

Gulati S, Riley FP, Hirsa AH, Lopez JM (2019) Flow in a containerless liquid system: ring-sheared drop with finite surface shear viscosity. Phys Rev Fluids 4(4):044006. https://doi.org/10.1103/PhysRevFluids.4.044006

Guo D, Xie G, Luo J (2014) Mechanical properties of nanoparticles: basics and applications. J Phys D Appl Phys 47(1):013001. https://doi.org/10.1088/0022-3727/47/1/013001

Guo MT, Rotem A, Heyman JA, Weitz DA (2012) Droplet microfluidics for high-throughput biological assays. Lab Chip 12(12):2146. https://doi.org/10.1039/c2lc21147e

Guo X, Chen X, Zhou W, Wei J (2022) Effect of polymer drag reducer on rheological properties of rocket kerosene solutions. Materials 15(9):3343. https://doi.org/10.3390/ma15093343

Heckbert PS, Hanrahan P (1984) Beam tracing polygonal objects. SIGGRAPH Comput Graph 18(3):119–127. https://doi.org/10.1145/964965.808588

Hofmann S, Weiland C, Fitschen J, von Kameke A, Hoffmann M, Schlüter M (2022) Lagrangian sensors in a stirred tank reactor: comparing trajectories from 4D-particle tracking velocimetry and Lattice-Boltzmann simulations. Chem Eng J 449:137549. https://doi.org/10.1016/j.cej.2022.137549

Hou J, Kaiser F, Sciacchitano A, Rival DE (2021) A novel single-camera approach to large-scale, three-dimensional particle tracking based on glare-point spacing. Exp Fluids 62(5):100. https://doi.org/10.1007/s00348-021-03178-8

Hoyer K, Holzner M, Lüthi B, Guala M, Liberzon A, Kinzelbach W (2005) 3D scanning particle tracking velocimetry. Exp Fluids 39(5):923–934. https://doi.org/10.1007/s00348-005-0031-7

Huang BK, Choma MA (2015) Microscale imaging of cilia-driven fluid flow. Cell Mol Life Sci 72(6):1095–1113. https://doi.org/10.1007/s00018-014-1784-z

Humphrey JAC, Hummel RL, Smith JW (1974) Experimental study of the internal fluid dynamics of forming drops. Can J Chem Eng 52(4):449–456. https://doi.org/10.1002/cjce.5450520403

Janke T, Schwarze R, Bauer K (2020) Part2Track: a MATLAB package for double frame and time resolved Particle Tracking Velocimetry. SoftwareX 11:100413. https://doi.org/10.1016/j.softx.2020.100413

Kaminski TS, Garstecki P (2017) Controlled droplet microfluidic systems for multistep chemical and biological assays. Chem Soc Rev 46(20):6210–6226. https://doi.org/10.1039/C5CS00717H

Kasagi N, Nishino K (1991) Probing turbulence with three-dimensional particle-tracking velocimetry. Exp Thermal Fluid Sci 4(5):601–612. https://doi.org/10.1016/0894-1777(91)90039-T

Kawaguchi M, Fukui T, Funamoto K, Tanaka M, Tanaka M, Murata S, Miyauchi S, Hayase T (2019) Viscosity estimation of a suspension with rigid spheres in circular microchannels using particle tracking velocimetry. Micromachines 10(10):675. https://doi.org/10.3390/mi10100675

Kim JT, Kim D, Liberzon A, Chamorro LP (2016) Three-dimensional particle tracking velocimetry for turbulence applications: case of a jet flow. JoVE 108(108):53745. https://doi.org/10.3791/53745

Kováts P, Thévenin D, Zähringer K (2018) Characterizing fluid dynamics in a bubble column aimed for the determination of reactive mass transfer. Heat Mass Transf 54(2):453–461. https://doi.org/10.1007/s00231-017-2142-0

Kvon AZ, Bobylev AV, Guzanov VV, Kharlamov SM (2020) Application of the PTV with the use of a light-field camera to study three-dimensional wave regimes of liquid film flow. J Phys Conf Ser 1677(1):012069. https://doi.org/10.1088/1742-6596/1677/1/012069

Landauer J, Tauwald SM, Foerst P (2019) A simple μ-PTV setup to estimate single-particle charge of triboelectrically charged particles. Front Chem 7:323. https://doi.org/10.3389/fchem.2019.00323

Lanzerotti MY, Brakke K, Allen K, Blackmon W, Hartke J, Hirsa AH (2021) Formation of a single drop of molten steel following bursting of liquid film in a vertical steel plate illuminated by a high energy laser. Appl Phys A 127(8):638. https://doi.org/10.1007/s00339-021-04680-w

Lee JCW, Porcar L, Rogers SA (2019) Unveiling temporal nonlinear structure-rheology relationships under dynamic shearing. Polymers 11(7):1189. https://doi.org/10.3390/polym11071189

Lei YC, Tien WH, Duncan J, Paul M, Ponchaut N, Mouton C, Dabiri D, Rösgen T, Hove J (2012) A vision-based hybrid particle tracking velocimetry (PTV) technique using a modified cascade correlation peak-finding method. Exp Fluids 53(5):1251–1268. https://doi.org/10.1007/s00348-012-1357-6

López CA, Lee CC, Hirsa AH (2005) Electrochemically activated adaptive liquid lens. Appl Phys Lett 87(13):134102. https://doi.org/10.1063/1.2058209

López CA, Hirsa AH (2008) Fast focusing using a pinned-contact oscillating liquid lens. Nat Photon 2(10):610–613. https://doi.org/10.1038/nphoton.2008.198

Ludwicki JM, Kern VR, McCraney J, Bostwick JB, Daniel S, Steen PH (2022) Is contact-line mobility a material parameter? npj Microgravity 8(1):6. https://doi.org/10.1038/s41526-022-00190-y

Maas HG, Gruen A, Papantoniou D (1993) Particle tracking velocimetry in three-dimensional flows: Part 1. Photogrammetric determination of particle coordinates. Exp. Fluids 15(2):133–146. https://doi.org/10.1007/BF00190953

Malik NA, Dracos T, Papantoniou DA (1993) Particle tracking velocimetry in three-dimensional flows part ii: particle tracking. Exp Fluids 15:279–294

Mallery K, Shao S, Hong J (2020) Dense particle tracking using a learned predictive model. Exp Fluids 61(10):223. https://doi.org/10.1007/s00348-020-03061-y

Malouin BA Jr, Vogel MJ, Olles JD, Cheng L, Hirsa AH (2011) Electromagnetic liquid pistons for capillarity-based pumping. Lab Chip 11(3):393–397. https://doi.org/10.1039/C0LC00397B

Marin AC, Grossi T, Bianchi E, Dubini G, Lacroix D (2017) *M*-Particle tracking velocimetry and computational fluid dynamics study of cell seeding within a 3D porous scaffold. J Mech Behav Biomed Mater 75:463–469. https://doi.org/10.1016/j.jmbbm.2017.08.003

Matsuura Y, Nakamura A, Kato H (2018) Nanoparticle tracking velocimetry by observing light scattering from individual particles. Sens Actuators B Chem 256:1078–1085. https://doi.org/10.1016/j.snb.2017.10.054

McBride SA, Tilger CF, Sanford SP, Tessier PM, Hirsa AH (2015) Comparison of human and bovine insulin amyloidogenesis under uniform shear. J Phys Chem B 119:10426–10433

McBride SA, Sanford SP, Lopez JM, Hirsa AH (2016) Shear-induced amyloid fibrillization: the role of inertia. Soft Matter 12:3461–3467

McMackin PM, Griffin SR, Riley FP, Gulati S, Debono NE, Raghunandan A, Lopez JM, Hirsa AH (2020) Simulated microgravity in the ring-sheared drop. npj Microgravity 6(1):2. https://doi.org/10.1038/s41526-019-0092-1

McGlynn JA, Wu N, Schultz KM (2020) Multiple particle tracking microrheological characterization: fundamentals, emerging techniques and applications. J Appl Phys 127(20):201101. https://doi.org/10.1063/5.0006122

McMackin P, Adam J, Griffin S, Hirsa A (2022) Amyloidogenesis via interfacial shear in a containerless biochemical reactor aboard the International Space Station. npj Microgravity 8(1):41. https://doi.org/10.1038/s41526-022-00227-2

McMackin PM, Adam JA, Griffin SR, Bonocora RP, Brakke KA, Lopez JM, Hirsa AH (2022) Effects of microorganisms on drop formation in microgravity during a parabolic flight with residual gravity and jitter. Microgravity Sci Technol 34(2):15. https://doi.org/10.1007/s12217-022-09933-8

Meyer F, Eigenbrod C, Wagner V, Paa W, Hermanson JC, Ando S, Avila M (2022) Oxygen droplet combustion in hydrogen under microgravity conditions. Combust Flame 241:112081. https://doi.org/10.1016/j.combustflame.2022.112081

Mujtaba B, de Lima JL (2018) Laboratory testing of a new thermal tracer for infrared-based PTV technique for shallow overland flows. CATENA 169:69–79. https://doi.org/10.1016/j.catena.2018.05.030

Murr LE, Johnson WL (2017) 3D metal droplet printing development and advanced materials additive manufacturing. J Market Res 6(1):77–89. https://doi.org/10.1016/j.jmrt.2016.11.002

Noto D, Tasaka Y, Murai Y (2021) In situ color-to-depth calibration: toward practical three-dimensional color particle tracking velocimetry. Exp Fluids 62(6):131. https://doi.org/10.1007/s00348-021-03220-9

Oeler KJ, Hill DB, Oldenburg AL (2021) OCT particle tracking velocimetry of biofluids in a microparallel plate strain induction chamber. J Biomed Opt 26(09):096005. https://doi.org/10.1117/1.JBO.26.9.096005

Parker JT, DeBerardinis J, Mäkiharju SA (2022) Enhanced laboratory X-ray particle tracking velocimetry with newly developed tungsten-coated O(50 *M*m) tracers. Exp Fluids 63(12):184. https://doi.org/10.1007/s00348-022-03530-6

Patel M, Leggett SE, Landauer AK, Wong IY, Franck C (2018) Rapid, topology-based particle tracking for high-resolution measurements of large complex 3D motion fields. Sci Rep 8(1):5581. https://doi.org/10.1038/s41598-018-23488-y

Pojman JA, Bessonov N, Volpert V, Paley MS (2007) Miscible fluids in microgravity (MFMG): A zero-upmass investigation on the International Space Station. Microgravity Sci Technol 19(1):33–41. https://doi.org/10.1007/BF02870987

Posada D, Tessier PM, Hirsa AH (2012) Removal versus fragmentation of amyloid-forming precursors via membrane filtration. Biotechnol Bioeng 109(3):840–845. https://doi.org/10.1002/bit.24341

Puzyrev D, Harth K, Trittel T, Stannarius R (2020) Machine learning for 3D particle tracking in granular gases. Microgravity Sci Technol 32(5):897–906. https://doi.org/10.1007/s12217-020-09800-4

Qureshi MH, Tien WH, Lin YJP (2021) Performance comparison of particle tracking velocimetry (PTV) and particle image velocimetry (PIV) with long-exposure particle streaks. Meas Sci Technol 32(2):024008. https://doi.org/10.1088/1361-6501/abb747

Reitz B, Lotz C, Gerdes N, Linke S, Olsen E, Pflieger K, Sohrt S, Ernst M, Taschner P, Neumann J, Stoll E, Overmeyer L (2021) Additive manufacturing under lunar gravity and microgravity. Microgravity Sci Technol 33(2):25. https://doi.org/10.1007/s12217-021-09878-4

Riley FP, McMackin PM, Lopez JM, Hirsa AH (2021) Flow in a ring-sheared drop: drop deformation. Phys Fluids 33(4):042117. https://doi.org/10.1063/5.0048518

Rizzardi LF, Kunz H, Rubins K, Chouker A, Quiriarte H, Sams C, Crucian BE, Feinberg AP (2016) Evaluation of techniques for performing cellular isolation and preservation during microgravity conditions. npj Microgravity 2(16025):1–10

Romano M, Alberini F, Liu L, Simmons M, Stitt E (2021) 3D-PTV flow measurements of Newtonian and non-Newtonian fluid blending in a batch reactor in the transitional regime. Chem Eng Sci 246:116969. https://doi.org/10.1016/j.ces.2021.116969

Romano M, Alberini F, Liu L, Simmons MJH, Stitt E (2023) Comparison between RANS and 3D-PTV measurements of Newtonian and non-Newtonian fluid flows in a stirred vessel in the transitional regime. Chem Eng Sci 267:118294. https://doi.org/10.1016/j.ces.2022.118294

Sabbagh R, Kazemi MA, Soltani H, Nobes DS (2020) Micro- and macro-scale measurement of flow velocity in porous media: a shadow imaging approach for 2D and 3D. Optics 1(1):71–87. https://doi.org/10.3390/opt1010006

Sampath K, Harfi TT, George RT, Katz J (2018) Optimized time-resolved echo particle image velocimetry-particle tracking velocimetry measurements elucidate blood flow in patients with left ventricular thrombus. J Biomech Eng 140(4):041010. https://doi.org/10.1115/1.4038886

Samuel H, Lognonné P, Panning M, Lainey V (2019) The rheology and thermal history of Mars revealed by the orbital evolution of Phobos. Nature 569(7757):523–527. https://doi.org/10.1038/s41586-019-1202-7

Satake Si (2022) Micro- and nanoscale imaging of fluids in water using refractive-index-matched materials. Nanomaterials 12(18):3203. https://doi.org/10.3390/nano12183203

Savorana G, Słomka J, Stocker R, Rusconi R, Secchi E (2022) A microfluidic platform for characterizing the structure and rheology of biofilm streamers. Soft Matter 18(20):3878–3890. https://doi.org/10.1039/D2SM00258B

Scheithauer U, Potschke J, Weingarten S, Schwarzer E, Vornberger A, moritz T, Michaelis A (2017) Droplet-based additive manufacturing of hard metal components by thermoplastic 3D printing (T3DP). J Ceram Sci Tech 08(01):155–160. https://doi.org/10.4416/JCST2016-00104

Schuöcker D, Aichinger J, Majer R (2012) Dynamic phenomena in laser cutting and process performance. Phys Procedia 39:179–185. https://doi.org/10.1016/j.phpro.2012.10.028

Sciacchitano A, Discetti S (2022) Special issue on uncertainty quantification in particle image velocimetry and Lagrangian particle tracking. Meas Sci Technol 33(1):010201. https://doi.org/10.1088/1361-6501/ac2c49

Shirley P (2020) Ray tracing in one weekend (3.2.3 ed.). CC0

Sokoray-Varga B, Józsa J (2008) Particle tracking velocimetry (PTV) and its application to analyse free surface flows in laboratory scale models. Period Pol Civ Eng 52(2):63. https://doi.org/10.3311/pp.ci.2008-2.02

Suresh R, Simranjeet S (2020) Exoplanets and their structure, rheology and dynamics. Int Res J Eng Tech 7(10):44–49

Tagliavini G, Khan MH, McCorquodale M, Westbrook C, Holzner M (2022) Wake characteristics of complex-shaped snow particles: comparison of numerical simulations with fixed snowflakes to time-resolved particle tracking velocimetry experiments with free-falling analogs. Phys Fluids 34(5):055112. https://doi.org/10.1063/5.0089759

Tamim SI, Bostwick JB (2021) Oscillations of a soft viscoelastic drop. npj Microgravity 7(1):42. https://doi.org/10.1038/s41526-021-00169-1

Tauro F, Piscopia R, Grimaldi S (2019) PTV-stream: a simplified particle tracking velocimetry framework for stream surface flow monitoring. CATENA 172:378–386. https://doi.org/10.1016/j.catena.2018.09.009

Toeneboehn K, Cooke ML, Bemis SP, Fendick AM, Benowitz J (2018) Stereovision combined with particle tracking velocimetry reveals advection and uplift within a restraining bend simulating the Denali fault. Front Earth Sci 6:152. https://doi.org/10.3389/feart.2018.00152

Torres LJ, Weislogel MM (2021) The ejection of large non-oscillating droplets from a hydrophobic wedge in microgravity. npj Microgravity 7(1):52. https://doi.org/10.1038/s41526-021-00182-4

Trantum JR, Eagleton ZE, Patil CA, Tucker-Schwartz JM, Baglia ML, Skala MC, Haselton FR (2013) Cross-sectional tracking of particle motion in evaporating drops: flow fields and interfacial accumulation. Langmuir 29(21):6221–6231. https://doi.org/10.1021/la400542x

Trinh EH, Depew J (1993) Sid surface wetting and the deployment of drops in microgravity. Appl Phys Lab 1:583–600

Tyson RK, Frazier BW (2022) Principles of adaptive optics, 5th edn. CRC Press, Taylor & Francis Group, Boca Raton London New York

Uemura T, Yamamoto F, Ohmi K (2012) A high speed algorithm of image analysis for real time measurement of a 2d velocity distribution flow visualization. Am Soc Mech Eng Fluids Eng Div 85:129–134

Vogel MJ, Steen PH (2010) Capillarity-based switchable adhesion. Proc Natl Acad Sci USA 107(8):3377–3381. https://doi.org/10.1073/pnas.0914720107

Wang IH, Burckhardt C, Yakimovich A, Greber U (2018) Imaging, tracking and computational analyses of virus entry and egress with the cytoskeleton. Viruses 10(4):166. https://doi.org/10.3390/v10040166

Wang G, Huang G, Gong X, Zhang G (2020) Method for 3D tracking behaviors of interplaying bacteria individuals. Opt Express 28(19):28060. https://doi.org/10.1364/OE.401032

Wang W, Lu B, Geng J, Li F (2020) Mesoscale drag modeling: a critical review. Curr Opin Chem Eng 29:96–103. https://doi.org/10.1016/j.coche.2020.07.001

Weislogel MM, Graf JC, Wollman AP, Turner CC, Cardin KJT, Torres LJ, Goodman JE, Buchli JC (2022) How advances in low-g plumbing enable space exploration. npj Microgravity 8(1):16. https://doi.org/10.1038/s41526-022-00201-y

Xu SH, Wang CX, Sun ZW, Hu WR (2011) The influence of contact line velocity and acceleration on the dynamic contact angle: an experimental study in microgravity. Int J Heat Mass Transf 54(9–10):2222–2225. https://doi.org/10.1016/j.ijheatmasstransfer.2011.01.018

Zhang Z, Hwang M, Kilbaugh TJ, Sridharan A, Katz J (2022) Cerebral microcirculation mapped by echo particle tracking velocimetry quantifies the intracranial pressure and detects ischemia. Nat Commun 13(1):666. https://doi.org/10.1038/s41467-022-28298-5

Zhao Y, Ma X, Zhang C, Wang H, Zhang Y (2020) 3D real-time volumetric particle tracking velocimetry—a promising tool for studies of airflow around high-rise buildings. Build Environ 178:106930. https://doi.org/10.1016/j.buildenv.2020.106930

Ziegenhein T, Garcon M, Lucas D (2016) Particle tracking using micro bubbles in bubbly flows. Chem Eng Sci 153:155–164. https://doi.org/10.1016/j.ces.2016.07.024